Title	A CFD investigation of a variable-pitch vertical axis hydrokinetic turbine with incorporated flow acceleration
Author(s)	Mannion, Brian; McCormack, Vincent; Leen, Sean B.; Nash, Stephen
Publication Date	2019-02-18
Publication Information	Mannion, Brian, McCormack, Vincent, Leen, Seán B., & Nash, Stephen. (2019). A CFD investigation of a variable-pitch vertical axis hydrokinetic turbine with incorporated flow acceleration. Journal of Ocean Engineering and Marine Energy, 5(1), 21-39. doi: 10.1007/s40722-019-00130-1
Publisher	Springer
Link to publisher's version	https://doi.org/10.1007/s40722-019-00130-1
Item record	http://hdl.handle.net/10379/15590
DOI	http://dx.doi.org/10.1007/s40722-019-00130-1

A CFD Investigation of a Variable-pitch Vertical Axis Hydrokinetic Turbine with Incorporated Flow Acceleration

Brian Mannion [1,*], Vincent McCormack[2], Seán B. Leen[1,] and Stephen Nash [1,*]

[1] College of Engineering & Informatics, National University of Ireland Galway, Ireland and SFI Centre for Marine Renewable Energy Ireland.
[2] GKinetic Energy LTD, Limerick, Ireland.
* Correspondence: b.mannion4@nuigalway.ie; stephen.nash@nuigalway.ie

Abstract: This paper presents the numerical modelling of a novel vertical axis tidal turbine that incorporates localised flow acceleration and variable-pitch blades. The focus is to develop a computational fluid dynamics model of a 1:20 scale model of the device using ANSYS® Fluent®. A nested sliding mesh technique is presented, using an outer sliding mesh to model the turbine and additional inner sliding meshes used for each of the six blades. The turbine sliding mesh is embedded in an outer static domain which includes the flow accelerating bluff body. Modelled power performance and velocity data are compared with experimental results obtained from scale model tests in a recirculating flume. The predicted power curves show general agreement with the measured data; the relative difference in maximum performance coefficient for example, is just 5.7 %. The model also accurately reproduces measured flows downstream of the turbine. The verified and experimentally validated model is subsequently used to investigate the effects of the variable-pitching and number of blades on device performance.

Keywords: Novel vertical axis tidal turbine; Performance prediction; Flow acceleration; Sliding mesh; Blade pitch control; Computational fluid dynamics.

1. Introduction

In recent times, significant research and development resources are being utilised in an effort to develop efficient tidal stream energy converters. To date, the majority of the research has primarily concentrated on horizontal axis tidal turbines; this is evident from the current market leaders in the sector such as Simec Atlantis Energy, Verdant Power, Andritz Hydro Hammerfest, Voith, OpenHydro and Scotrenewables, whose turbines are all horizontal axis designs. Although there are some examples of vertical axis tidal turbines (e.g. Instream Energy Systems, New Energy Corporation, HydroQuest, and Norwegian Ocean Power), they have not been investigated to the same extent.

Numerical models for performance prediction and design optimisation have become imperative to the successful development of commercial-scale hydrokinetic devices. Several numerical modelling approaches of varying complexity and accuracy have been developed, but there are three primary model types: (1) blade element momentum theory models, (2) free-vortex models and (3) computational fluid dynamics models.

Blade Element Momentum Theory (BEMT) was initially developed by the research contributions of Glauert (1926), Strickland (1975) and Templin (1974). It is based on a combination of blade element and momentum theories through the use of the well-documented actuator disc and stream tube approaches. The strength of this approach is its relatively low computational cost compared to other methods. BEMT models allow for rapid evaluation of turbine design iterations. The majority of BEMT models require an iterative approach to determine the local axial induction factor and depend on experimental aerofoil data or data that has been predicted using a panel method (e.g. XFOIL®); the work of Sheldahl and Klimas (1981) is a commonly used data set. BEMT is most useful for devices with low blade loadings and/or low solidity, and devices that operate at lower tip speed ratio ranges; for highly loaded turbines, the implementation of the iterative approach in determining the axial induction factor can result in convergence issues (Gupta and Leishman, 2005; Klimas and Sheldahl, 1978; Paraschivoiu et al., 1983; Strickland, 1975). Free-vortex models are based on the representation of the aerofoil blade as a bound vortex filament, called a lifting line. This lifting line changes its magnitude as the azimuthal position varies (Ponta and Jacovkis, 2001). Strickland et al. (1979) were the first to successfully implement a vortex model in relation to a (wind) turbine. Blade forces are calculated within the free-vortex model using the blade element method (BEM) based on experimental aerofoil data, and the forces are applied with knowledge of blade local velocity vectors.

Although the BEMT and free-vortex model approaches can be used as early stage design evaluation tools, when accuracy is paramount, the method most commonly used throughout research and industry is CFD. The governing equations of flow in CFD models are the Navier-Stokes equations, and a number of approaches are used to solve them including Direct Numerical Simulation (DNS), Large Eddy Simulation (LES), Detached Eddy Simulation (DES), and the Reynolds Averaged Navier-Stokes (RANS) approach. Direct Numerical Simulation (DNS) involves the complete 3D and time-dependent solution of the Navier-Stokes and continuity equations. However, due to the massive computational expense associated with DNS modelling, it is currently restricted to very simple geometries and is therefore not a viable option for turbine modelling. Large Eddy Simulation (LES) is a technique where the large eddies are directly computed without. The conservation equations are not averaged in time, but rather are averaged in space. The small-scale turbulence is diluted and contributes less to the Reynolds stresses, and is therefore not as vital. Turbulence modelling is then reduced to only the sub-grid scale. However, even with the application of a wall-treatment (sub-grid scale model). Significant difficulties occur for LES near solid surfaces where eddies are small, to the extent that the stress-bearing and dissipation ranges of eddy size overlap. This means that the spatial and temporal refinement near solid surfaces increases to that required for full DNS. The Detached Eddy Simulation (DES) method was developed as a computational cost-reducing method that treats large eddies using conventional LES, while treating boundary layers and thin shear layers with the conventional RANS approach.

The RANS approach is commonly used to model complex turbulent flows such as flow through a turbine. This time-averaged approach requires the use of a turbulence model to compute the Reynolds stresses. The most commonly used turbulence models include the Spalart-Allmaras (Spalart et al., 1992), $k - \varepsilon$ (Launder and Spalding, 1974), $k - \omega$ (Wilcox, 1988), $k - \omega$ shear stress transport (SST) (Menter, 1994) and Transitional SST models (Menter et al. 2006). The Transitional SST model incorporates two additional equations, in addition to the, k and ω equations of the $k - \omega$ SST model, intermittency (γ) and the transitional momentum thickness Reynolds number ($\overline{Re}_{\theta t}$). γ is used to determine whether the Transitional SST model should be active. When γ equals zero, the production of turbulent kinetic energy, k is suppressed and the flow is effectively laminar. When γ is equal to one, the Transitional SST model is fully active and the flow is assumed to be fully turbulent. $\overline{Re}_{\theta t}$ controls the transition criterion between laminar and turbulent flow. The critical Reynolds number, $Re_{\theta c}$, occurs where intermittency begins to increase in the boundary layer. It occurs upstream of the Reynolds number of transition onset, $Re_{\theta t}$, as turbulence must first build up to appreciable levels in the boundary layer before any change in the laminar profile can occur. As a result, $Re_{\theta c}$ is the location where turbulence starts to grow and $Re_{\theta t}$, is the location where the velocity profile starts to deviate from a purely laminar profile. Further information on the Transitional SST is available in the developers research Langtry & Menter (2009); Menter et al. (2006) or the ANSYS Fluent 17.1 theory guide (2016).

The software used to implement the RANS equations in this research is ANSYS® Fluent®; it is commonly used in turbine modelling. ANSYS® Fluent® was chosen for this research over other code such as Star CCM and OpenFOAM for example, as Fluent allows adequate flexibility and robustness for the development of a variable pitch turbine model. Fluent also has an extensive user-defined function library for adaptation to many problems and scenarios. CFD models of turbines can be steady-state or transient. If computational resources are scarce, steady-state models can be applied for turbine blades at different azimuthal positions and the results aggregated (Masters et al., 2015). Transient modelling of the moving blades, although more complicated, is more accurate and is important where blade interaction occurs, e.g. for high solidity devices like the turbine studied in this research. Transient modelling techniques require the simulation to explicitly represent the turbine blade movement through the fluid. This can be accomplished using a sliding mesh techniques (Korobenko et al., 2013; Lain and Osorio, 2010; Lee et al., 2015) where one part of the mesh moves while the remainder is static. The sliding mesh technique is adapted here to facilitate variation in blade pitch by nesting inner higher resolution sliding meshes within an outer lower resolution sliding mesh.

The vertical axis hydrokinetic turbine which is the focus of this research was developed by GKinetic Energy Ltd. A 3D image of the device is shown in Figure 1(a), while a picture of the device during field tests is presented in Figure 1(b). The device has two vertical axis turbines positioned either side of a central bluff body. Two significant features of the device are: (1) the central *bluff body* accelerates the entrance velocities to the turbines and (2) the variable-pitching turbine blades that are designed to maximise hydrodynamically induced torque on the generator shaft. Scaled prototypes of the turbine have been tested in a recirculating flume (Mannion, et al. 2018a) and in the field.

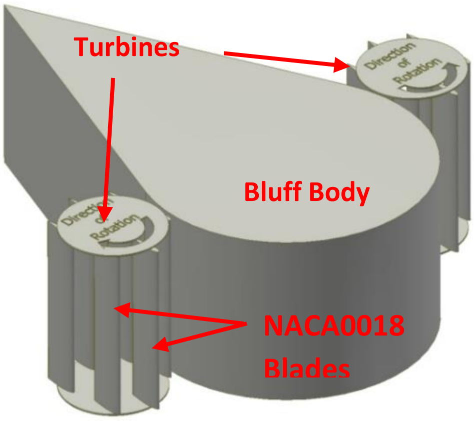

(**a**)

(**b**)

Figure 1: (a) Solid model of the GKinetic tidal turbine; **(b)** photograph of the deployed device. Reproduced with permission from Mannion, et al. (2018a).

This paper presents the development of a 2D transient CFD model of the turbine shown in Figure 1 using a nested sliding mesh technique. The model includes the flow accelerating bluff body and variable blade pitching; the latter is controlled during simulations via a user-defined function (UDF). The developments are based on CFD modelling recommendations and best practice identified from the literature. The model is used to simulate 1:20 scale model tests conducted in a recirculating flume. The predicted performance is validated by comparison with measured data for mechanical power and wake velocities. The converged and experimentally validated model is used to investigate various aspects of the current device setup including the number of blades on the turbines, the benefits variable versus fixed pitch blades, shaft sizing, location of turbine relative to the bluff body and the effect of blade chord length. Each of the design cases is assessed in relation to mechanical power performance.

2. Methodology

2.1. Device background and experimental testing

As seen in Figure 1, the hydrokinetic device comprises of two vertical axis turbines (VATs), each of which has six NACA 0018 profile blades of 200 mm chord length. For VATs, the angle of attack varies widely during each revolution of the turbine, so symmetrical profiles are most commonly used. Furthermore, in the present device, when the blades of the turbine are transitioning from upstream to downstream, they undergo a sudden 70^{o} change in pitch angle which made symmetrical blade profiles more desirable. Thinner profiles exhibit larger lift to drag ratios (Sheldahl and Klimas, 1981), but NACA 0018 profiles were chosen for this particular turbine due to their stiffness due to bending over the thinner profiles of NACA 0012 and NACA 0015.

Variable-pitching was implemented using a patented cam track and follower controlling each blade via individual shafts.

The experimental data used to validate the CFD model was collected during testing of a 1:20 scale model in the IFREMER recirculating flume in Boulogne-sur-Mer, France. The flume measures 18 m long, 4 m wide and 2.1 m deep and is capable of producing flow velocities in the range of 0.1 to 2.2 m/s. Due to the dimensional constraints of the tank, it was only feasible to test half of the device, i.e. one-half of the bluff body and a single turbine, the dimensions of which are shown in Figure 2. The mechanical power, P_m, was calculated from measured torque and rotational speed and converted to a power coefficient (C_{P}) using:

$$C_{\mathrm{P}} = \frac{P_m}{0.5\rho A {U_\infty}^3} \tag{1}$$

where ρ is water density, A is device entrance area (i.e. the sum of the bluff body and turbine entrance areas), and U_∞ is freestream velocity. More detail on the experimental testing is available in Mannion, et al. (2018a).

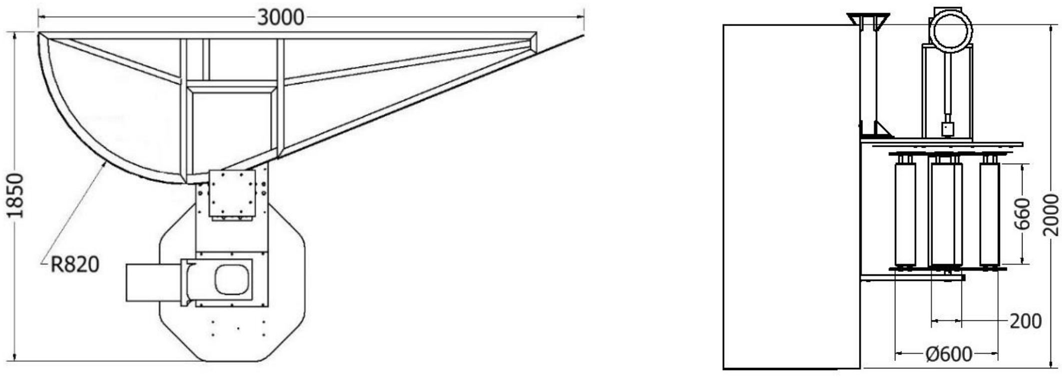

(a) **(b)**

Figure 2: 1:20 scale device with outlining dimensions (mm); **(a)** plan view **(b)** end elevation. Reproduced with permission from Mannion, et al. (2018a).

2.2. CFD Modelling Considerations

There are many differences between previously published CFD sliding mesh turbine model studies. Mesh refinement (e.g. number of nodes over hydrofoils edges), diameter of rotating domain relative to turbine diameter and extents of the domain upstream and downstream of the turbine all vary widely. Domain width also varies; in some cases, it is restricted to the extents of the experimental domain (Bachant and Wosnik, 2016) while other studies define domain sizes relative to blade chord length (Almohammadi et al., 2012). A 2D model which retains the same domain extent as a test setup presents a higher blockage ratio than the test. Mannion et al. (2018b) showed that this higher blockage of the 2D model could lead to performance over-prediction. They also showed that such blockage errors can be corrected by extending the width of the 2D model domain to give the same blockage ratio as the test (Mannion et al. 2018b). This approach is implemented here so that the width of the domain is extended from 4 m to 5.633 m (Figure 3).

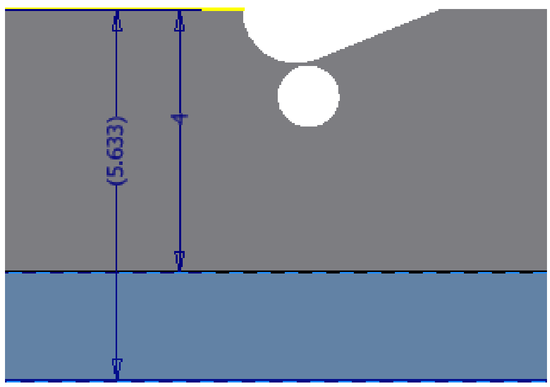

Figure 3: Blockage correction, distance to model wall extended from 4 m to 5.633 m.

The dimensionless wall distance, y^+, is an essential parameter in turbulence modelling as it helps determine the appropriate mesh resolution near solid boundaries. Values vary between studies but can be estimated for use with the selected turbulence model. Mohamed (2012) employs the $k - \varepsilon$ model for a VAT and recommend a $y^+ > 30$. However, logarithmic-based wall functions are not recommended where flow separation is likely, such as for VATs. Instead, either a $k\text{–}\omega$ based model or a Spalart-Allmaras based model can be used and the viscous sublayer directly resolved using $y^+ \cong 1$. Maître et al. (2013) followed this recommendation with the $k\text{–}\omega$ SST.

2nd order spatial discretisation schemes are most commonly used in the literature and have shown to provide accurate model results. There is no general agreement on the best Fluent® solver for VAT modelling. All four available solvers have been implemented: SIMPLE (Semi-Implicit Method for Pressure-Linked Equations) (Mohamed, 2012), SIMPLEC (Semi-Implicit Method for Pressure-Linked Equations-Consistent) (Lam and Peng, 2016), PISO (Pressure-Implicit with Splitting of Operators) (Ghasemian and Nejat, 2015) and COUPLED (pressure-velocity coupling method), (Balduzzi et al., 2016) which is used in this research.

Confirmation of model convergence is crucial for CFD model credibility. The Richardson extrapolation is an example of a method used for determining CFD model convergence based on error estimating (Almohammadi et al., 2013). The Richardson extrapolation is used in this work to access mesh convergence. Whereas the number of rotations required for convergence is determined based on variation in the average torque loading of the rotor between subsequent rotations. In the literature the number of rotations for convergence has been found to vary, likely due to the turbine design, but is generally found to lie between 8 to 15 rotations (Chatterjee and Laoulache, 2013; Maître et al., 2013). The general consensus is that a solution is converged if the difference between the torque values of successive rotations is less than 1 %.

Another parameter that can have a significant effect on accuracy is the model time-step. It is essential to carry out temporal (and spatial) discretisation studies in order to achieve an entirely independent solution. It is common practice to normalise time-step values to correspond with azimuthal sizing. The value of time-step required for an independent solution is found to vary significantly. (Rossetti and Pavesi, 2013) found that a time-step representative of 2^o azimuth rotation per time-step is required for solution independence while other researchers such as Maître et al. (2013) and Trivellato and Raciti Castelli, (2014) suggest smaller time-step values of 1^o and less than 0.5^o, respectively. Balduzzi et al. (2016) show that smaller time-step values are required in cases of low flow speeds where large separation regions occur.

3. Model development

The 1:20 scale testing was conducted at a range of flow speeds, but model development and validation runs were limited to flow speeds of 0.7 m/s and 1.1 m/s. Table 1 presents a summary of the key dimensions of the CFD model and the 1:20 scale test device.

3.1. Mesh Geometry

The CFD mesh was developed using ANSYS® Workbench Meshing and predominately consists of unstructured triangular elements with quadrilateral elements at the walls. As shown in Figure 4, the model contains eight nested meshes in total. The outermost domain is static and contains the half-bluff body. The large outer sliding mesh, measuring 0.9 m in diameter, represents the turbine which has a diameter of 0.6 m. Nested within the turbine sliding mesh are six smaller sliding meshes of 0.29 m diameter, each of which represents one of the individual blades of 0.2 m chord length. Figure 5(a) shows the mesh for the full turbine, which is more refined closer to the hydrofoil walls; Figure 5(b) displays the full width of the static mesh where the size of the device in relation to the size of the domain is visible. Figure 6 shows an image of this converged mesh around one of the hydrofoils. The 35 quad element inflation layers are visible with a growth rate of 1.2.

Table 1. Key details and dimensions of 1:20 tidal turbine and associated CFD model domain details.

Description	Value
Turbine diameter (D)	0.6 m
Blade rotating mesh diameter	0.290 m
Turbine rotating mesh diameter	0.9 m
Blade profile type	NACA 0018

Blade chord (c)	0.2 m
Blade length (L)	0.667 m
Number of blades	6
Bluff body radius (BBR)	0.82 m
Bluff body length (BBL)	3 m

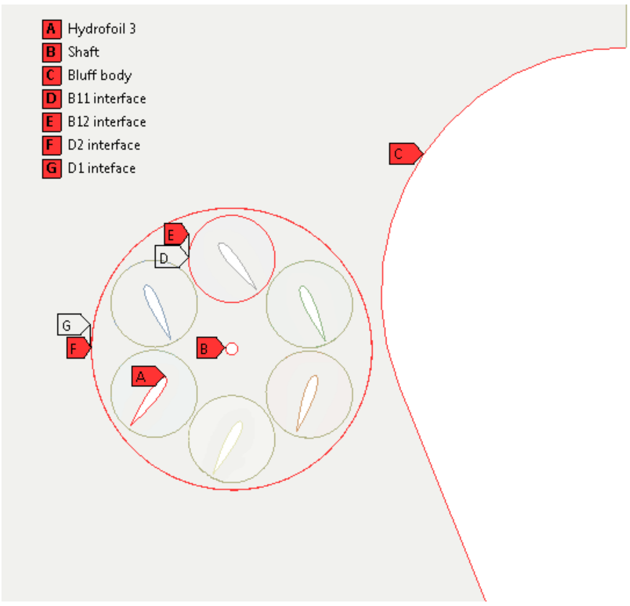

Figure 4: Schematic showing the arrangement of the model meshes with crucial components identified.

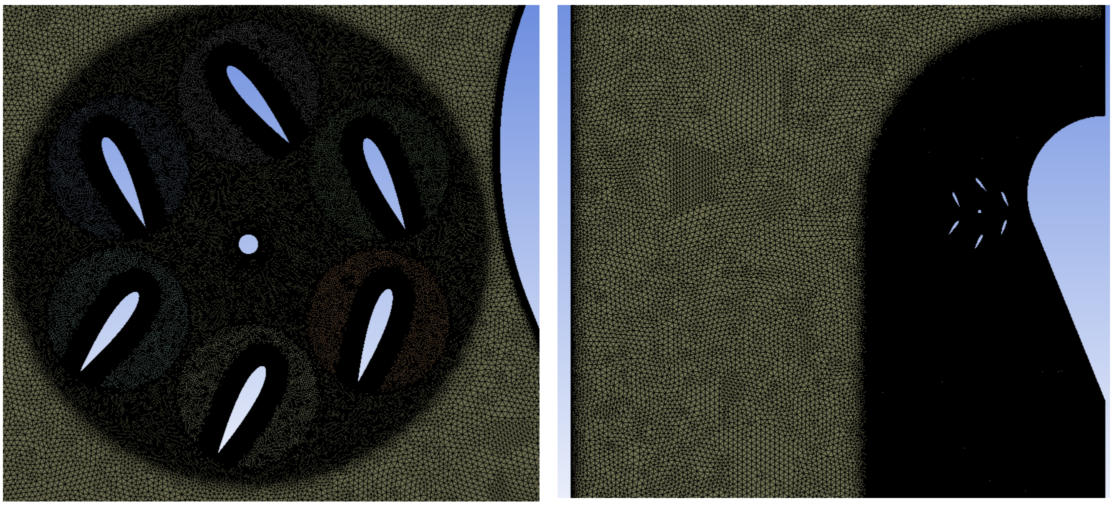

(a) (b)

Figure 5: Mesh showing **(a)** around turbine and **(b)** far field.

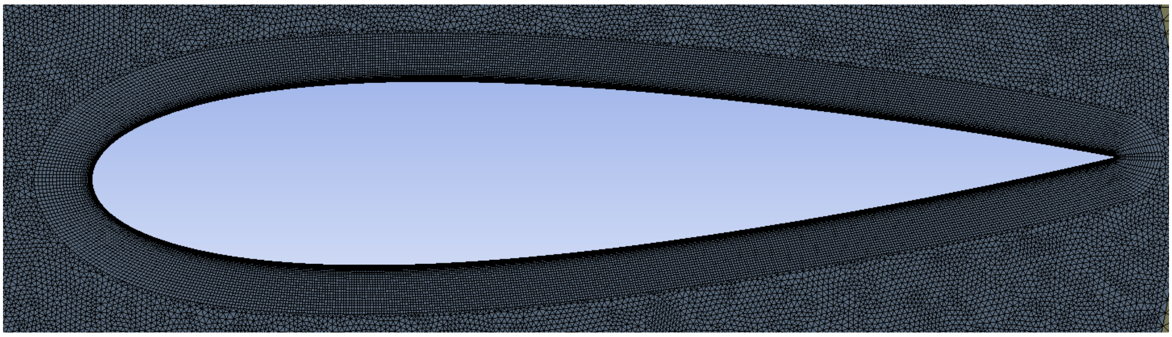

Figure 6: Mesh around hydrofoil with 35 quad inflation layers visible.

It was shown in Mannion, et al. (2018b) that while model results were sensitive to the turbine sliding mesh size, the effects were negligible once the diameter of the turbine rotating mesh was greater than 1.5 times the turbine diameter. In the present study, the sizes of the sliding meshes were restricted by dimensional constraints of the device setup. As can be seen in Figure 5(a), the presence of the bluff body (i.e. a wall boundary) next to the turbine restricted the turbine mesh size, while the chord length and the extents of the turbine sliding mesh restricted the size of the blade meshes. In both cases, however, the sliding mesh diameter was 1.5 times greater than the turbine diameter / chord length. Turbulence intensity was set at 5 % to be reflective of that present in the experimental testing. The lateral walls of the tank were considered as no-slip boundary walls.

3.2. Blade Pitch Control

Figure 7 presents a graphical illustration of the pitching of each of the six blades at an instance in time. In this orientation, the turbine rotates anticlockwise. It can be seen that the blade pitch changes as the blades turn along the up-stream (front) end of the turbine; this is due to the gradients in velocity magnitude and direction as one moves outwards from the bluff body. There is also a noticeable difference in the pitch of the blades on the down-stream side of the turbine compared to their up-stream pitch positions. Between position 3 and position 4, the blade undergoes a pitch transition of about 70° where the angle of attack changes from positive to negative. This location was chosen for this large transition (or flip) to minimise the turbulence generated in doing so. The reason for the flip is because the blades were found to contribute more power from drag than lift when turning through the down-stream portion of the cycle. To incorporate variable-pitching into the CFD model, the motion of the sliding meshes containing the blades had to be controlled. Each blade follows the same pitching profile within each turbine rotation. Mathematical expressions were developed to represent the pitching of the blades at each azimuthal position. A user-defined function (UDF) written in the C programming language was used to control the motion of the individual blade domains and is able to account for different turbine rotational velocities. The model was implemented on a Linux 48 node cluster.

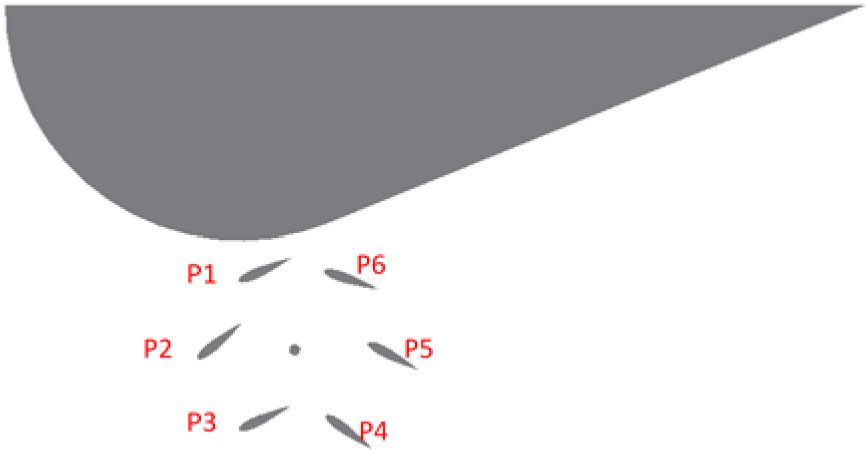

Figure 7: Schematic of turbine blade pitching relative to the bluff body. Reproduced with permission from Mannion, et al. (2018a).

3.3. Mesh Convergence Study

The mesh sensitivity study required the development of several different meshes of varying densities (Table 2). As is seen in the table, the method of increasing the mesh densities was to increase the number of nodes along the edges of the hydrofoils (identified as "A" in Figure 4 and "No. of nodes along edges of hydrofoils" in Table 2). The number of elements along the domain interface edges was increased by increasing the number of divisions. The edges on both sides of the domain were selected to ensure the elements on either side of the interface corresponded; the interfaces are shown in Figure 4 as D and E ("Blade interface No. of divisions" in Table 2) for an inner rotating domain and F and G ("Turbine interface No. of divisions" in Table 2) for the outer rotating domain. Face sizing was also adjusted when mesh refinement was required. The number of quadrilateral/prism layers off the blade are referred to in the table as "No. of Quad rows" where a growth rate of 1.2 was used.

Table 2. Mesh parameters for sensitivity analysis.

	No. of nodes along edges of hydrofoils	No. of Quad rows	Turbine interface No. of divisions	Blade interface No. of divisions
M1	400	20	200	200
M2	550	25	400	250
M3	700	35	600	300
M4	850	35	800	350
M5	1000	35	1000	400

The Richardson extrapolation is used to calculate the exact solution based on the convergence and refinement ratio determined using a series of increasingly refined meshes. Before applying the Richardson extrapolation, it is necessary to determine the apparent convergence condition based on the R^*, defined as:

$$R^* = \frac{\phi_{\mathrm{grid}_2} - \phi_{\mathrm{grid}_1}}{\phi_{\mathrm{grid}_3} - \phi_{\mathrm{grid}_2}} \quad (2)$$

where ϕ is the parameter used for convergence, T in this case.

The following conditions apply:

- $R^*>1$ Monotonic divergence
- $1 > R^* > 0$ Monotonic convergence
- $0 > R^* > -1$ Oscillatory Convergence
- $R^* < -1$ Oscillatory divergence

Richardson extrapolation may only be used when the apparent convergence condition is monotonic. A constant mesh refinement ratio, r, is defined as:

$$r = \left(\frac{N_{\text{fine}}}{N_{\text{coarse}}}\right)^{\frac{1}{2}} \tag{3}$$

where N_{fine} is the number of elements in the fine mesh and N_{coarse} is the number of elements in the coarse mesh. The order of convergence, p is defined as:

$$p = \frac{\ln\left(\frac{T_{\text{grid}_2} - T_{\text{grid}_1}}{T_{\text{grid}_3} - T_{\text{grid}_2}}\right)}{\ln(r)} \tag{4}$$

The Richardson's extrapolation value is calculated as follows:

$$T = T_{\text{grid}_1} + \frac{T_{\text{grid}_1} - T_{\text{grid}_2}}{r^p - 1} + HOT \tag{5}$$

where HOT is for any higher order terms.

Figure 8 presents the variation of the five meshes in terms of predicted turbine torque. It is clear that mesh M4 was the most suitable as it provides a converged solution (within 1 % of the final Richardson's extrapolation value in Table 3) whilst minimising the computational cost. More specific spatial details of the M4 mesh are presented in Table 4. Figure 9 shows the variation of average and maximum y^+ evaluated over the duration of a full rotation.

Table 3. Mesh refinement convergence determined with Richardson's extrapolation

	No. of mesh elements ($\mathbf{x10^6}$)	**Modelled Torque (Nm)**	**Richardson's Value**	**Difference in Torque**
M1	0.5	240.47	141.25	-70.24%
M2	0.75	194.92	141.25	-37.99%
M3	0.9	162.07	141.25	-14.74%
M4	1.1	142.26	141.25	-0.72%
M5	1.3	141.10	141.25	0.11%

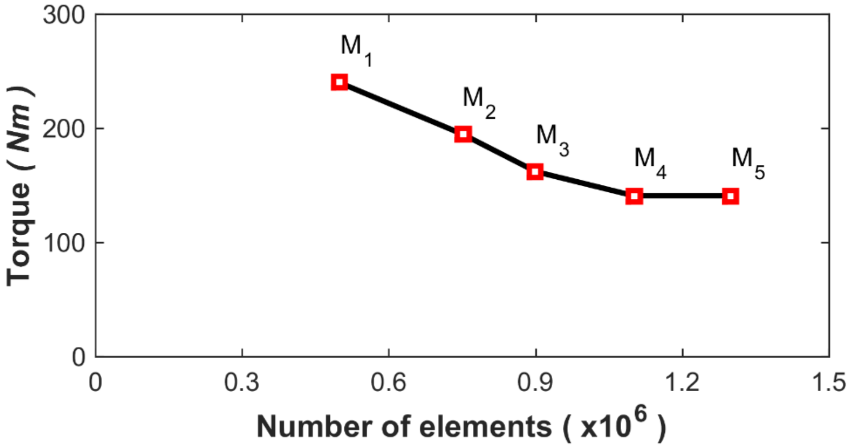

Figure 8: Mesh convergence study, showing M4 mesh as optimum for the model.

Table 4. Converged M4 mesh details.

Description	Value
Average skewness	0.0059
Max skewness	0.81
Average quality	0.86
Max aspect ratio	65
Max y^{+}	1.06
Number of elements	1.1 x $\mathbf{10^6}$

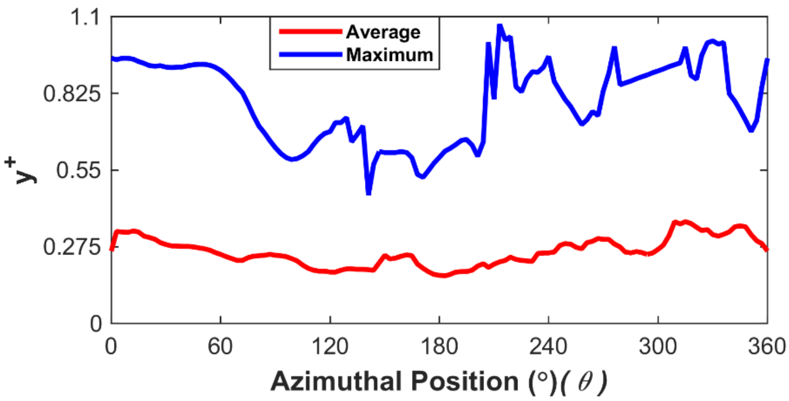

Figure 9: Average and maximum y^{+} evaluated over the duration of a full rotation.

3.4. Solution Convergence

The model solution is achieved in three stages. First, a moving reference frame (MRF) steady-state approach with 1st order discretization schemes is run for 10,000 iterations. Upon completion, the model is changed to transient and *mesh motion* continuing with the 1st order schemes until torque has reached a quasiperiodic state (usually after three to four rotations). At this stage, the model is changed to 2nd order schemes for the remainder of the calculation. This progressive approach was used to define the flow around the device adequately and to eliminate any potential divergence issues that may have arisen from using 2nd order schemes and sliding meshes at start-up. The coupled solver was used throughout this process.

The criteria for the number of rotations required for a converged solution was set to $\overline{\Delta T} < 0.1$ % between one rotational torque average and the next, where T is the torque; this was based on recommendations by Balduzzi et al (2016). Table 5 shows that 14 rotations were required for this criteria to be met.

Table 5. Number of rotations required for convergence.

Turbine Rotation	Torque (Nm)
1	260
4	155
8	143.7
13	141. 35
14	141.22

3.5. Temporal Convergence Study

A time-dependence study was carried out for a range of model timesteps. Balduzzi et al. (2016) showed that smaller time-steps are required for lower tip speed ratios (TSR or λ). Therefore, the lowest TSR value of 0.15 was chosen for the time convergence study as the most conservative case. The model was run using a number of different time-steps and torque was again compared across simulations. The independence study was undertaken at a flow speed of 1.1 m/s. A graph of the results is presented in Figure 10. It is clear from the figure that the model requires a small time-step in order to obtain an independent solution. This is most likely due to the complexity of the model with seven moving meshes and the high spatial resolutions. Based on the study, a time-step value coinciding to 0.2 azimuthal degrees per time-step ($°/\Delta t$) was identified as optimum for this TSR and was used across all TSRs.

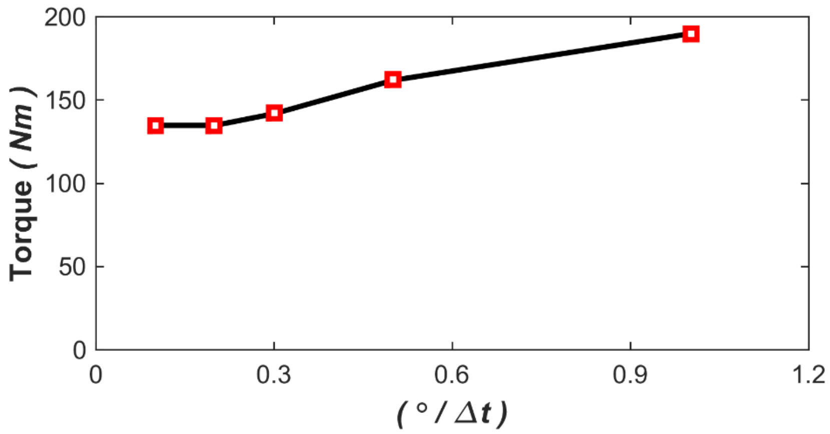

Figure 10: The time-step study, showing optimum time step representing 0.2° per time step.

3.6. Design iterations investigation

The validated model was used to investigate the effects of design decisions on device performance. The CFD results from the current device setup (Figure 11(a)) are used as a baseline against which all other device setups are compared. The following design decisions are investigated.

1. Turbine position: the present turbine location relative to the static parts of the device was chosen based on experimental studies of flow acceleration around the bluff body (Mannion, et al. 2018a) which found that

maximum localised flow acceleration occurred at the widest point of the bluff body. To investigate whether this is indeed the optimum position for the turbine, two models are used where the turbine is moved downstream from its present position by 100 mm and 200 mm (parallel to the flume).

2. Shaft diameter: It is well understood that larger diameter shafts generate more turbulence and vorticity than smaller diameter shafts. As the current device has a 40 mm diameter shaft, additional analyses for shaft diameters of 15 mm and 80 mm were investigated.
3. Blade pitching and number of blades: The effects of (i) a fixed 0° pitch (both 3 and 6-bladed) and (ii) a 3-bladed device with the same variable-pitch regime as the 6-bladed case were investigated. Small numbers of blades (usually 2-3) are typical on VATS.
4. Hydrofoil chord length: a model consisting of 0.15 m chord length hydrofoils is compared with the current 0.2 m chord length hydrofoils. Both models use NACA 0018 hydrofoils.

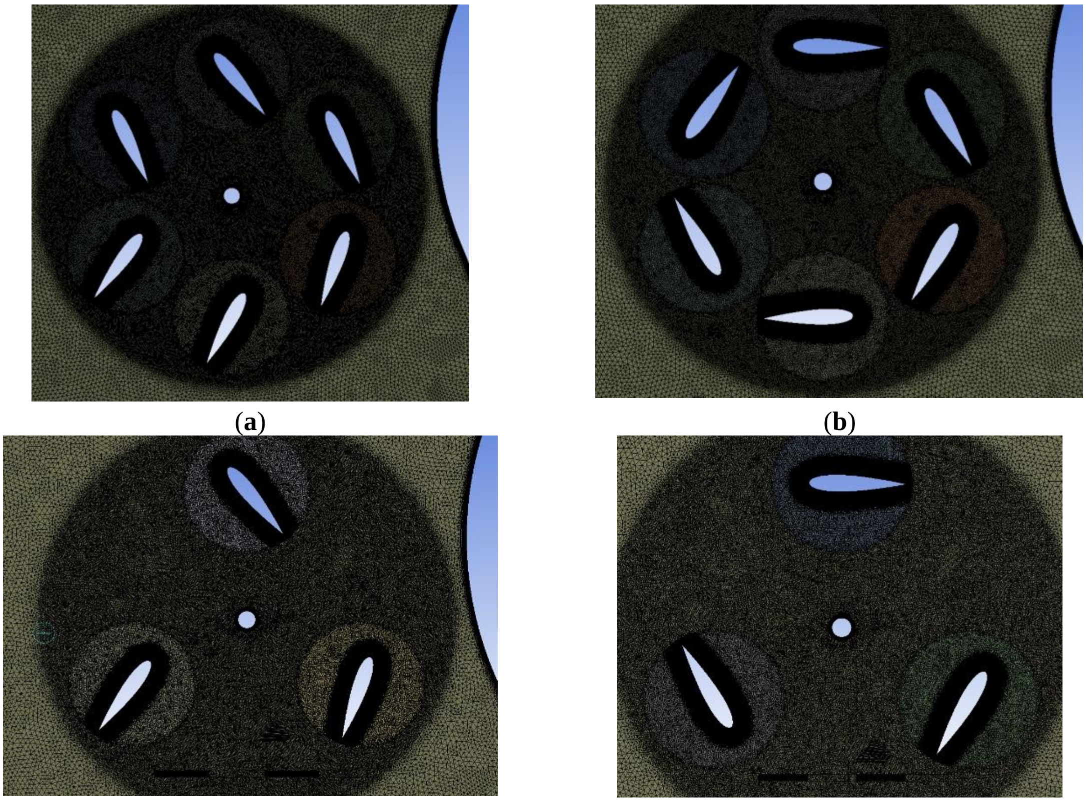

(a) (b) (c) (d)

Figure 11: Images of meshes used for carrying out investigation of performance for **(a)** baseline model experimental setup, **(b)** 6 bladed 0° fixed pitched **(c)** 3 bladed variable-pitched and **(d)** 3 bladed 0° fixed pitched.

4. Results

CFD-predicted power coefficients and downstream flow velocities are presented in this section and compared with measured experimental data for model validation, including a comparison of the two SST turbulence models and the study.

4.1. Model Validation for Power Coefficient

Power performance of the turbine is assessed using the power coefficient, C_{P}. A common method for calculation of C_{P} from CFD simulations uses the average moment coefficient ($\overline{C_m}$) (see Equation (6)) over a rotation multiplied by the tip speed ratio (λ). For cases where the freestream velocity is accelerated before entering the turbine, as in this work, an alternative approach is required. Instead, the torque is output after the completion of each time-step and averaged and C_{P} is then calculated according to Equation (7). Figure 12 presents a comparison of modelled C_{P} versus λ using the two different turbulence models with the measured data for an ambient flow speed of 1.1 m/s.

$$\overline{C_{\mathrm{m}}} = \frac{\bar{M}}{0.5\rho A {U_{\infty}}^{2} L} \tag{6}$$

where $\bar{M}$ is the average turning moment (Torque) created around a predefined axis, i.e. the centre of the turbine, and L is the reference length (taken as the turbine radius).

$$C_{\mathrm{P}} = (\overline{C_{\mathrm{m}}})(\lambda) = \frac{\bar{T}\omega}{0.5\rho A {U_{\infty}}^{3}} \tag{7}$$

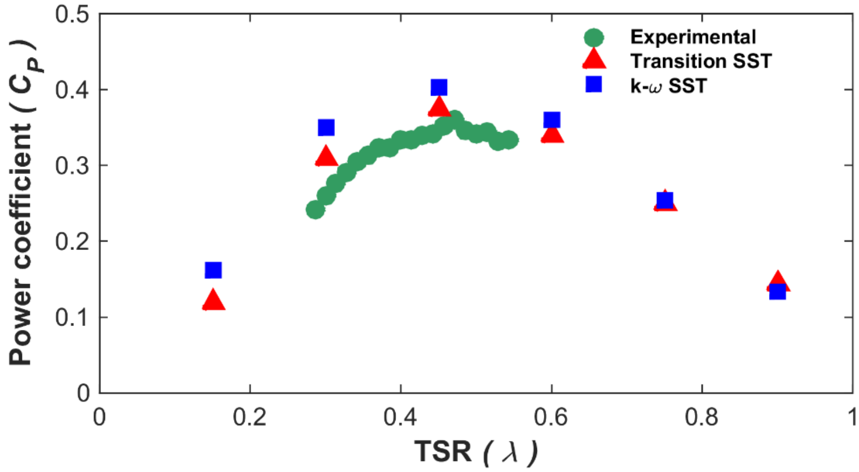

Figure 12: Power curve comparison between experimental and CFD at U_{∞} equal to 1.1 m/s.

It can be seen that both models performed well in predicting the peak and overall trend of the power curve. The test data recorded a $C_{\mathrm{P}max}$ of 0.35 at a TSR of 0.46, and both CFD models predicted the $C_{\mathrm{P}max}$ to occur at a TSR of 0.45. The results from the Transitional SST model are more accurate than those from the $k - \omega$ SST model. For $C_{\mathrm{P}max}$ the difference in modelled and measured values for the Transitional SST model was just 5.7 % while the difference was 14 % for the $k - \omega$ SST model. The more accurate Transitional SST model was also subsequently further investigated for an ambient flow speed of 0.7 m/s. Figure 13 shows the comparison of the modelled and measured power curves (U_{∞} equal to 0.7 m/s). In this case, the model is accurate to within 10 % for $C_{\mathrm{P}max}$ and the general trends are again in agreement.

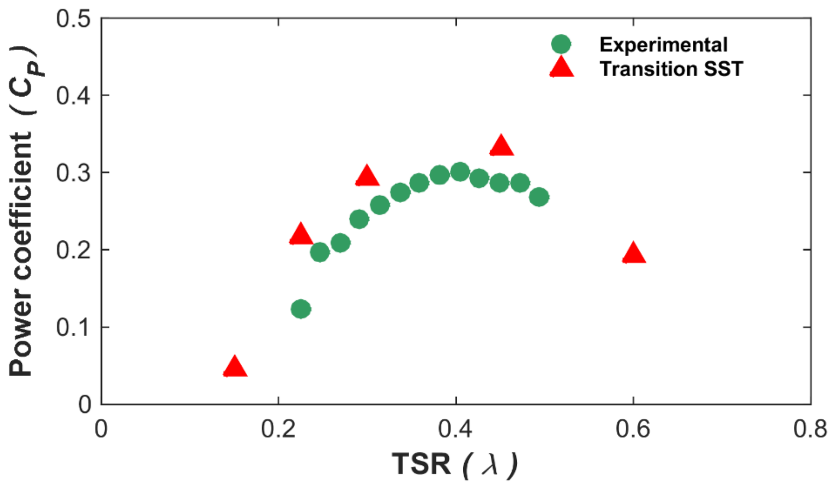

Figure 13: Power curve comparison between experimental and CFD at U_∞ equal to 0.7 m/s.

Figure 14 and Figure 15 present velocity contour plots (at U_∞ equal to 1.1 m/s) after 14 rotations from the two different turbulence model simulations. The two plots clearly show the complexity of the flow through and around the device. The flow accelerator, blade pitching and high solidity of the device are some of the reasons why such a complex flow is formed.

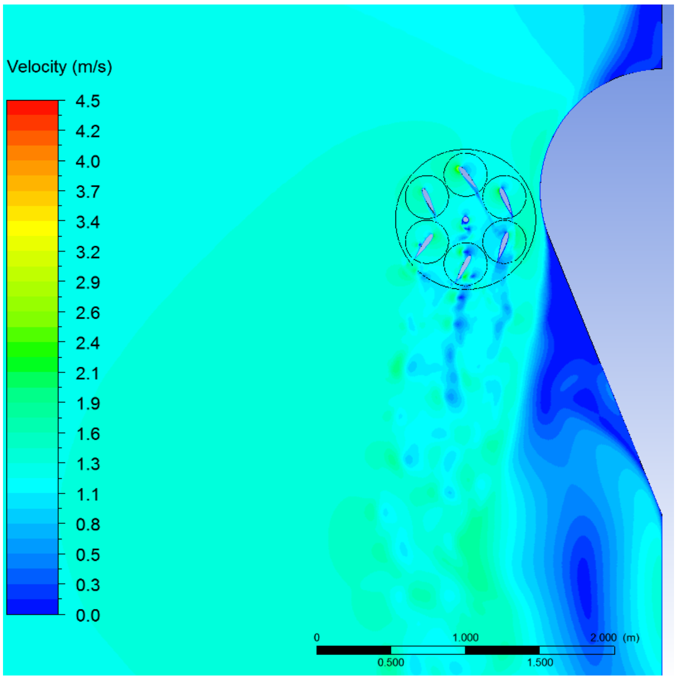

Figure 14: Transition SST velocity contour map around the device at 1.1 m/s.

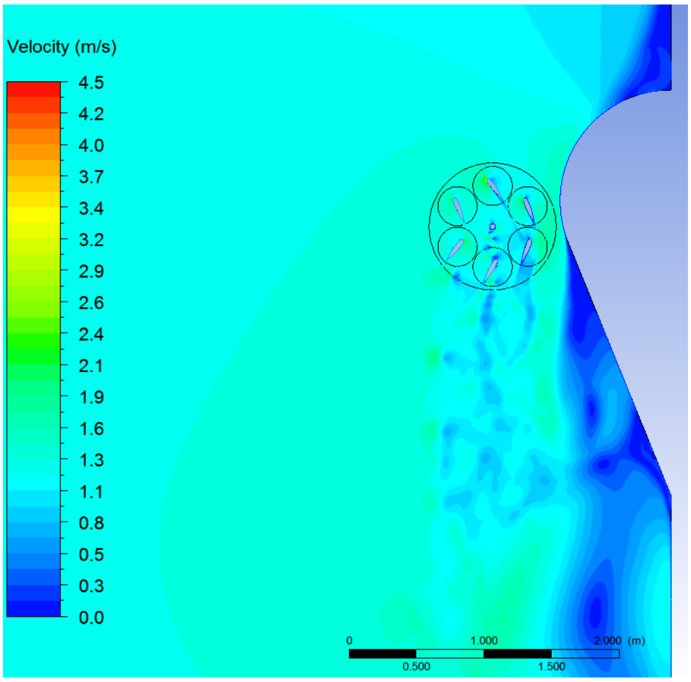

Figure 15: $k-\omega$ SST velocity contour map around the device at 1.1 m/s.

4.2. Model Validation for Downstream Velocities

During the scale tests, flow velocities were measured using a laser Doppler velocimetry (LDV) system at a free-stream velocity of 0.8 m/s. Due to restrictions in the movement of the LDV system, it was only possible to obtain LDV data along two transects downstream of the turbine. The velocities measured at mid-turbine depth are presented in the form of a velocity vector plot in Figure 16. Velocities are clearly reduced in the wake of the turbine and flow reversal is evident adjacent to the bluff body due to the generation of turbulent eddies. By way of further model validation, the model was rerun at 0.8 m/s and predicted velocities were compared with the measured data in Figure 17 and Figure 18, along transects A-A and B-B, respectively. Model data were extracted at every grid cell along the relevant transects. For clarity, these data are presented as line graphs instead of data points. Again, the Transitional SST model is shown to be more accurate. Both of the model datasets contain some velocity fluctuations not present in the measured data, but they are lower in the Transitional SST model. Given the complexity of the downstream flows shown in Figure 14 and Figure 15, the level of agreement achieved by the Transitional SST model is very encouraging. The model accurately predicts both the reductions in wake velocities and the flow reversal due to the presence of turbulent eddies. Table 6 presents the root mean squared errors (RMSE) for the wake velocity data predicted by the two turbulence models, These values were determined at the same locations as the LDV data.

Table 6. RMSE values for predicted velocity data along transects A-A and B-B.

	Transitional SST RMSE (m/s)	$k-\omega$ SST RMSE (m/s)
Transect A-A	0.13	0.38
Transect B-B	0.10	0.21

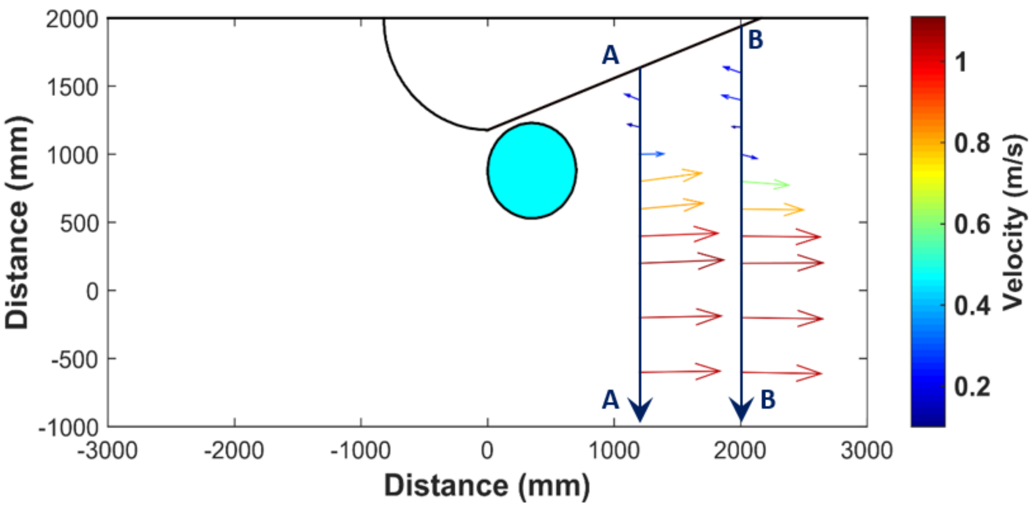

Figure 16: Vector plot of LDV experimental flow data for transects A-A and B-B.

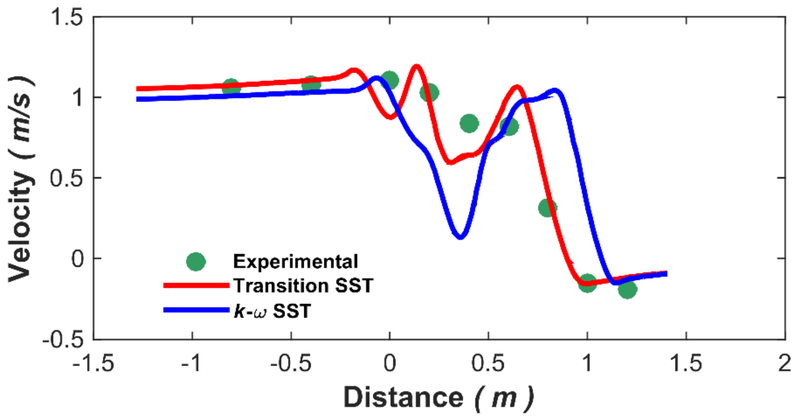

Figure 17: Velocity comparison between SST models and experimental data along transect A-A.

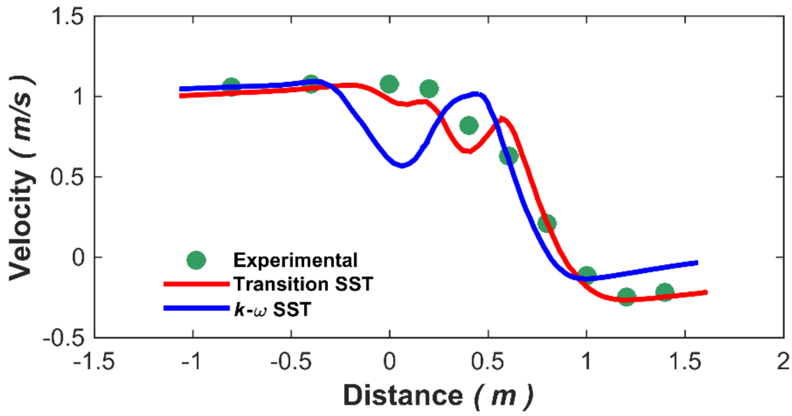

Figure 18: Velocity comparison between SST models and experimental data along transect B-B.

Contours of the turbulent kinetic energy (k) for each of the SST turbulence models are presented in Figure 19. The significantly more chaotic distribution of the turbulent kinetic energy predicted by the $k - \omega$ SST model is consistent with the greater velocity fluctuations for this model observed in Figure 17 and Figure 18.

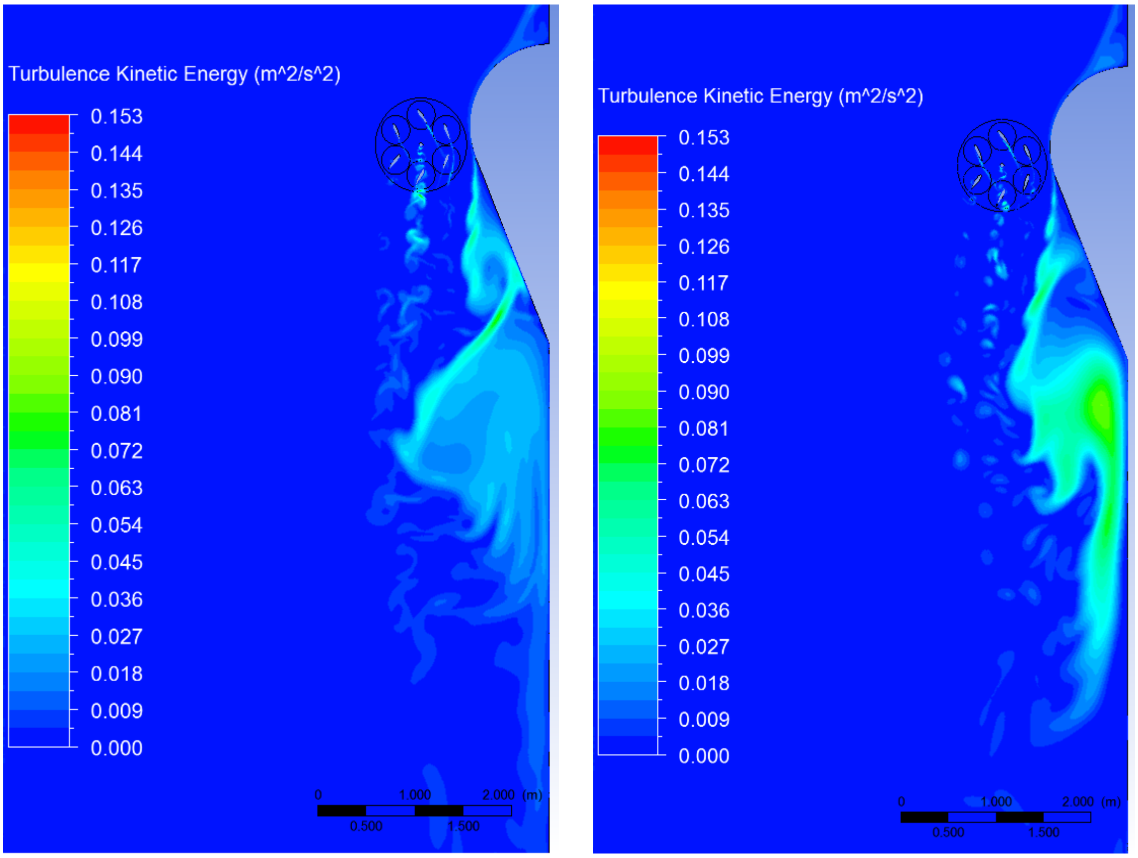

(**a**) (**b**)

Figure 19: Contour plots for turbulence kinetic energy from **(a)** Transition SST **(b)** $k-\omega$ SST models.

4.3. Design Investigation Study Results

The results of the convergence studies and model performance validation confirmed that the model was sufficiently accurate for design study purposes. The following sections present the results of the design study, all of which was conducted using the Transitional SST model at 1.1 m/s. the baseline results were taken from Figure 12.

4.3.1. Turbine Position

In the present design, the turbine position relative to the bluff body was determined from an experimental study of flow around a scale model of the bluff body conducted in a tidal basin (Mannion, et al. 2018a). Obviously, the flow around the bluff body will be different with the turbine in place. To determine whether the turbine is in the optimum position, two additional simulations were conducted with the turbine moved 100 mm and 200 mm downstream (parallel to the flume walls) to determine if the flow is fully developed prior to reaching the turbine inlet. Figure 20 compares the C_{P} values for the new turbine positions with those from the turbine in its current position (Baseline case). The Baseline case is seen to give the highest C_{P}; $C_{\mathrm{P}max}$ is 6.5 % and 12 % lower for the 100 mm and 200 mm downstream positions, respectively. Figure 21 compares velocity contour maps for the three cases. Although there are subtle differences between each case, it is not possible to conclude why the performance reduces on moving the turbine; one possible explanation is that the present cam control history for each pitch angle is designed for the current turbine position and is not optimal for the other cases. It is also possible that there is more space between the turbine and the bluff body. Further investigation of the figures through the use of difference plots confirmed minimal differences, with the exception of the locations of the downstream vortices which varied between setups. Stronger vortices to the right of the turbine, for both cases when the turbine was moved, were observed in comparison to the baseline case. It is probable that these enhanced vortices are the result of the increased distance between the turbine and bluff body.

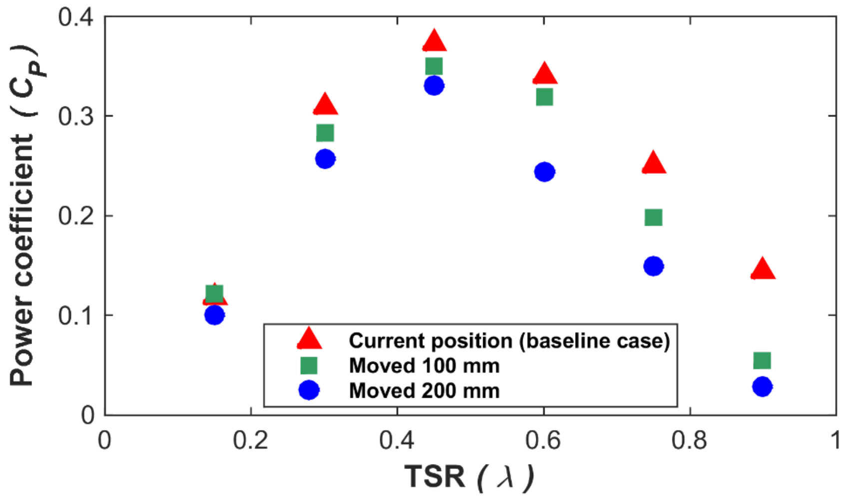

Figure 20: Comparison of power curves for three different turbine positions.

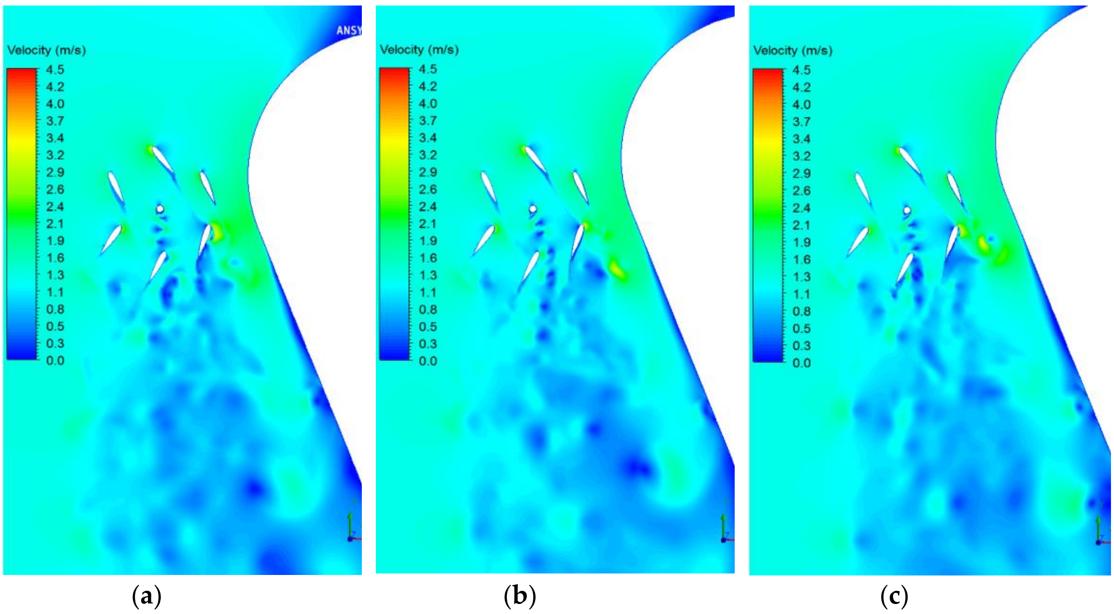

Figure 21: Velocity contour plots for different turbine positions behind the widest part of the bluff body for shifted positions of **(a)** 0 mm **(b)** 100 mm and **(c)** 200 mm, relative to static parts parallel to the flume.

4.3.2. Shaft Diameter

For VATs, larger turbine shafts create increased turbulence and vorticity on the incoming flow for the downstream blades. The current device uses a shaft of 40 mm diameter. To determine the effect of shaft size, additional model simulations were carried out for shaft diameters of 15 mm and 80 mm. Figure 22 compares values with that of the current design. As expected, use of the 15 mm shaft results in the highest $C_{\mathrm{P}max}$ value while the 80 mm gives the lowest. Use of the 80 mm results in a 10 % reduction in $C_{\mathrm{P}max}$ compared to the 15 mm shaft. Figure 23 presents contour maps of velocities in the vicinity of the turbine for the three design cases. For the 15 mm case, the shaft wake is quite confined in width but as the shaft diameter increases, it can be seen that the vortex street generated by the shaft spreads over an increasingly wider region, thereby impacting on more of the downstream blades and enhancing the parasitic nature to performance.

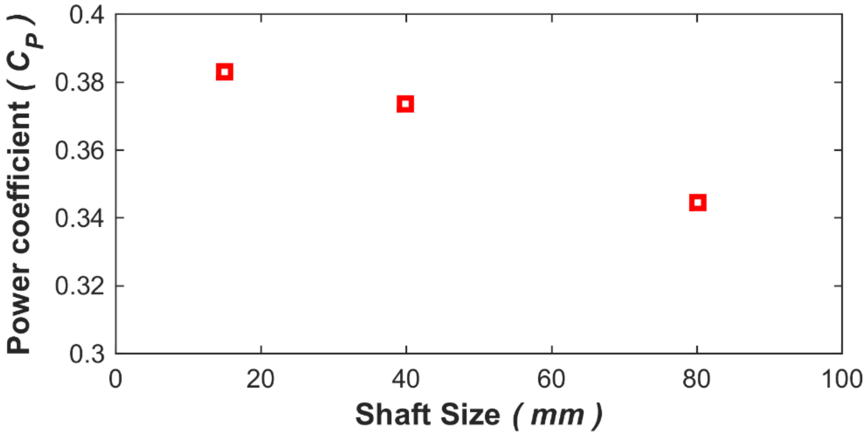

Figure 22: Power performance coefficient for turbine against turbine shaft diameter.

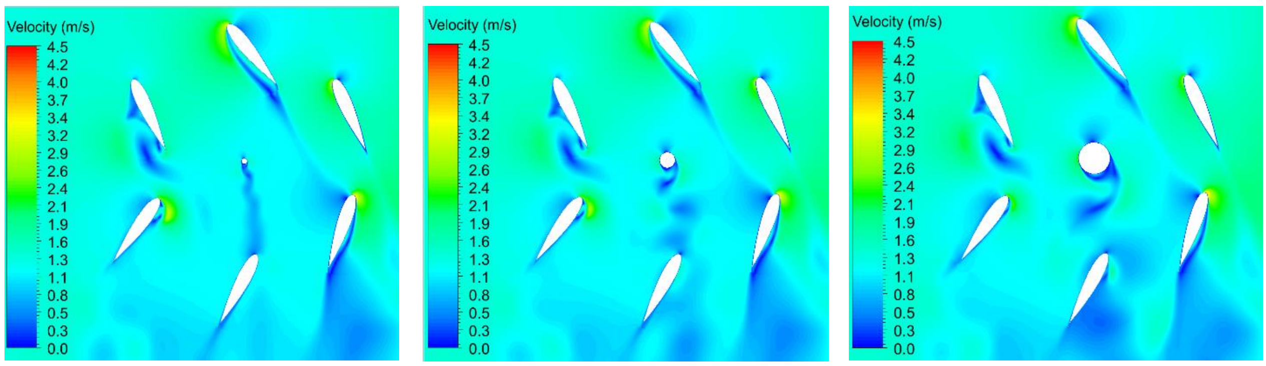

(**a**) (**b**) (**c**)

Figure 23: Velocity contour map for various turbine shaft diameters: **(a)** 15 mm **(b)** 40 mm and **(c)** 80 mm.

4.3.3. Blade Pitching and number of blades

The benefit of the pitching blades was investigated using an additional simulation where the turbine was modelled as a 0^{o} fixed pitch turbine. The effect of device solidity was also investigated by replacing the 6-blade turbine with a 3-blade turbine for both the variable and fixed pitch scenarios. The variable-pitch control specified for the 3-bladed turbine was the same as that used for the current 6-blade turbine. Figure 24 compares the power curves for these cases. The present 6-bladed variable-pitch setup is denoted as the baseline case.

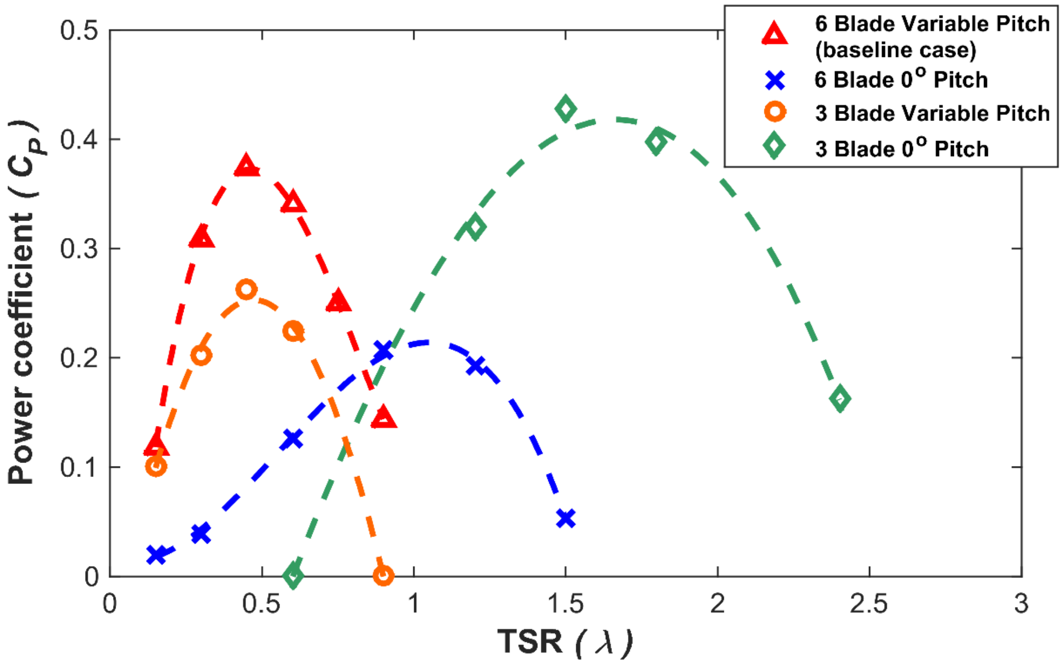

Figure 24: Comparison of variation in power coefficient of the parametric study of three and six-bladed turbines and variable-pitched vs 0^{o} fixed pitched turbines.

Comparison of the 6-blade variable-pitch baseline case and the 6-blade 0º fixed pitch case shows the beneficial effect of the variable-pitch regime; it results in an increase in C_{Pmax} from 0.21 to 0.37 and significantly reduces the optimum TSR for C_{Pmax} from 0.9 to 0.45. The 3-blade variable-pitch case shows significantly lower performance than the 6-blade case (C_{Pmax} of 0.26 compared to 0.37). This may be due to the fact that the blade pitch control scheme had been optimised for peak performance to be achieved at a low TSR value, at this speed the blades of the 3-bladed turbine rotate too slowly relative to the flow and the majority of the flow passes through the turbine without interacting with the blades. The 3-blade 0^{o} fixed pitch case achieves approximately 5 % higher C_{Pmax} than the baseline case, although at a much higher optimum TSR (λ = 1.7 versus λ = 0.45).

Figure 25 to Figure 28 present velocity contour and vector plots for the four different design cases at their relevant optimum TSR value. Comparing Figure 25 (6-blade, variable-pitch) and Figure 26 (6-blade, fixed pitch), it is clear that the high solidity of the 6-blade 0^{o} fixed pitch turbine causes significant blockage. The bulk of the flow is directed around the turbine without any beneficial blade interactions resulting in lower power performance. This is also demonstrated by the very low velocities inside the turbine in the vector plot of Figure 26(b). The directions of the vectors show that the majority of the flow is passing around the turbine, rather than through it, as a result of the excessive turbine solidity.

Comparing the 3-blade variable-pitch case of Figure 27 to those of the current 6-blade variable-pitch case (Figure 25), the instantaneous velocities immediately around the hydrofoils are seen to be quite similar; however, the contour maps show very different wakes. The area of high velocity immediately downstream of the 3-blade case suggests little power extraction from the flow on the right side of the turbine. A lot of the flow passes through without interacting with the blades. This is also where the highest inlet velocities are experienced. Much of the available power is, therefore, being lost and power extraction is lower. Comparing the velocity plots of the 3-blade 0^{o} fixed pitch case in Figure 28 to those of the baseline model of Figure 25, it can be seen that the peak velocities of the 3-blade 0^{o} fixed case are significantly higher than those of the 6-blade baseline case; this is likely due to the fact the TSR is much higher. Also, the velocity deficits in the wake of the 3-blade 0^o fixed case are more significant than those of the baseline case and could be significant in terms of proximity of devices in array deployments.

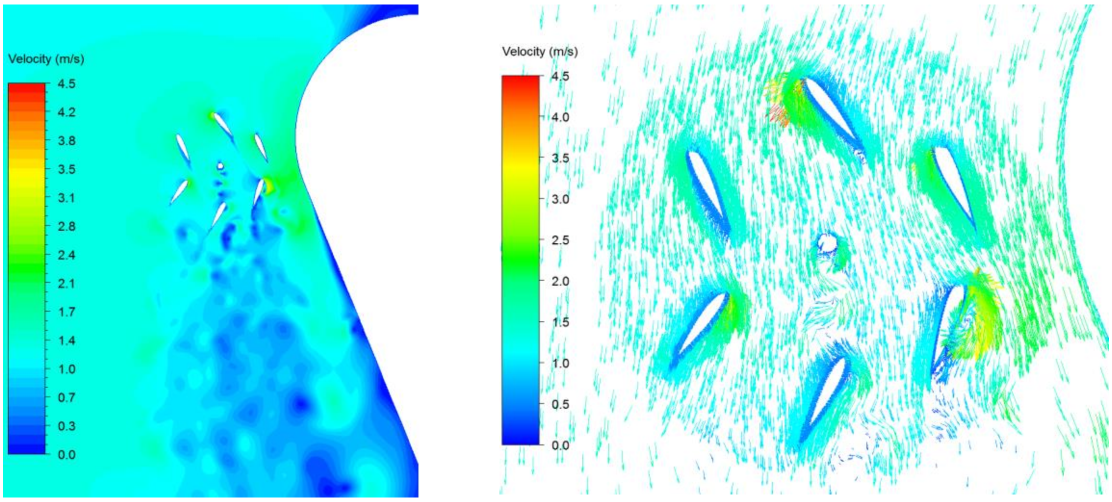

(**a**) (**b**)

Figure 25: Velocity plot of baseline case for (a) contour and (b) vector plot at optimum TSR of 0.45.

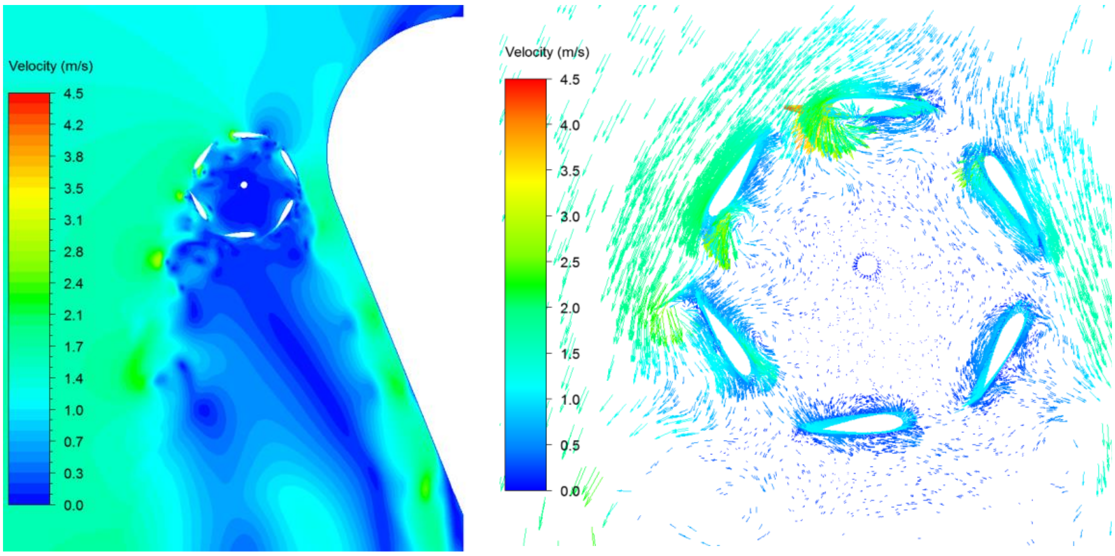

(**a**) (**b**)

Figure 26: Velocity plot of 6-bladed 0^o fixed pitch case for **(a)** contour and **(b)** vector plot at optimum TSR of 0.9

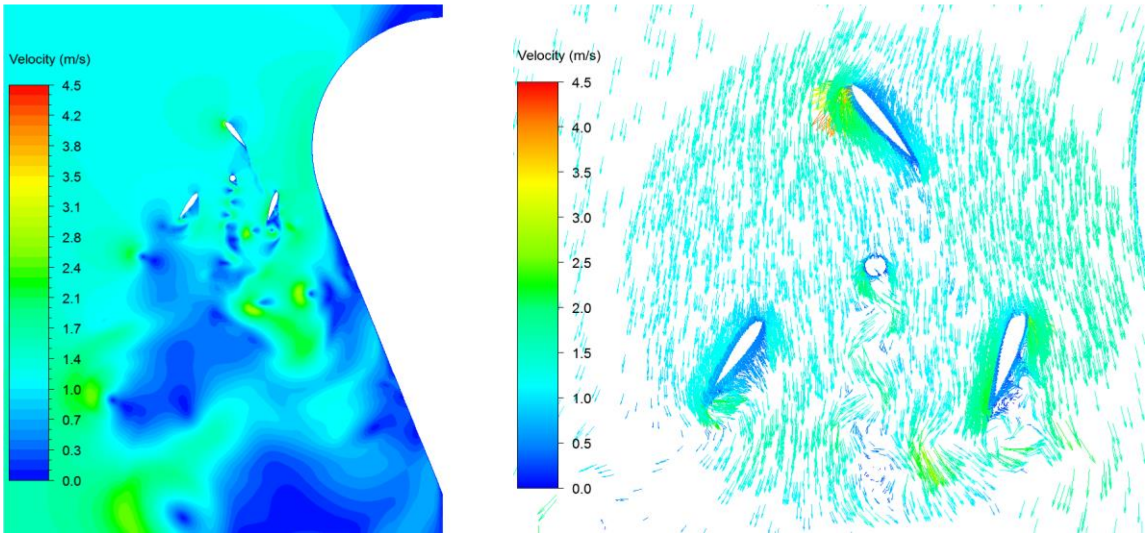

(**a**) (**b**)

Figure 27: Velocity plot of 3-bladed variable-pitch case for **(a)** contour and **(b)** vector plot at optimum TSR of 0.45.

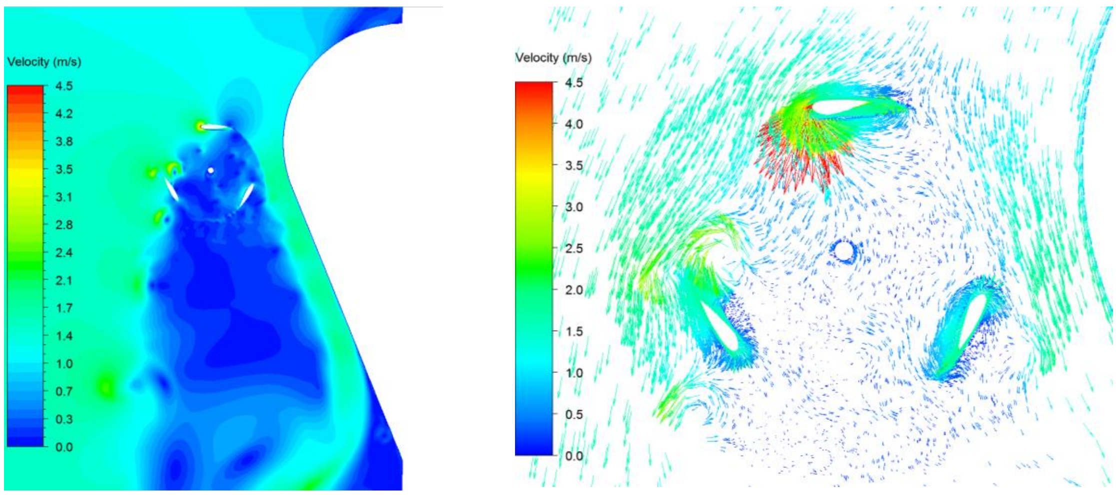

(**a**) (**b**)

Figure 28: Velocity plot of 3-bladed 0^{o} fixed pitch case for **(a)** contour and **(b)** vector plot at optimum TSR of 1.5.

4.3.4. Effect of chord length

An investigation was conducted to determine the effect of shorter chord lengths (0.15 m versus the current 0.2 m) on device performance. It was hypothesised that a shorter chord would reduce the solidity of the device and allow more flow to pass through the turbine. Figure 29 presents the comparison of the power curves for both cases. The baseline case achieves a higher performance throughout the TSR range with increase in C_{P} with TSR. Use of the 0.15 m chord results in a 10.5 % reduction in $C_{\mathrm{P}max}$. Figure 30 presents velocity contour maps (at a TSR of 0.45) from the 0.2 m chord and 0.15 m chord models, denoted in the figure as (a) and (b), respectively. Unfortunately, the contour maps do not exhibit many dissimilarities that could explain the difference in C_{P}; however, at this TSR value, there is only a 4 % difference in C_{P} between the cases.

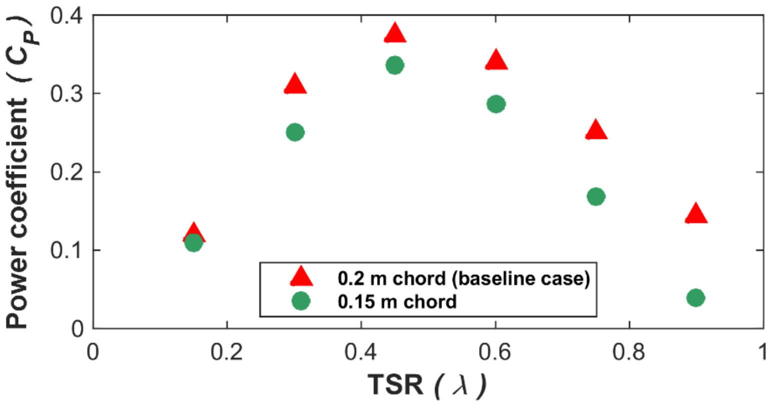

Figure 29: Comparison of turbine performance for two different hydrofoil chord lengths.

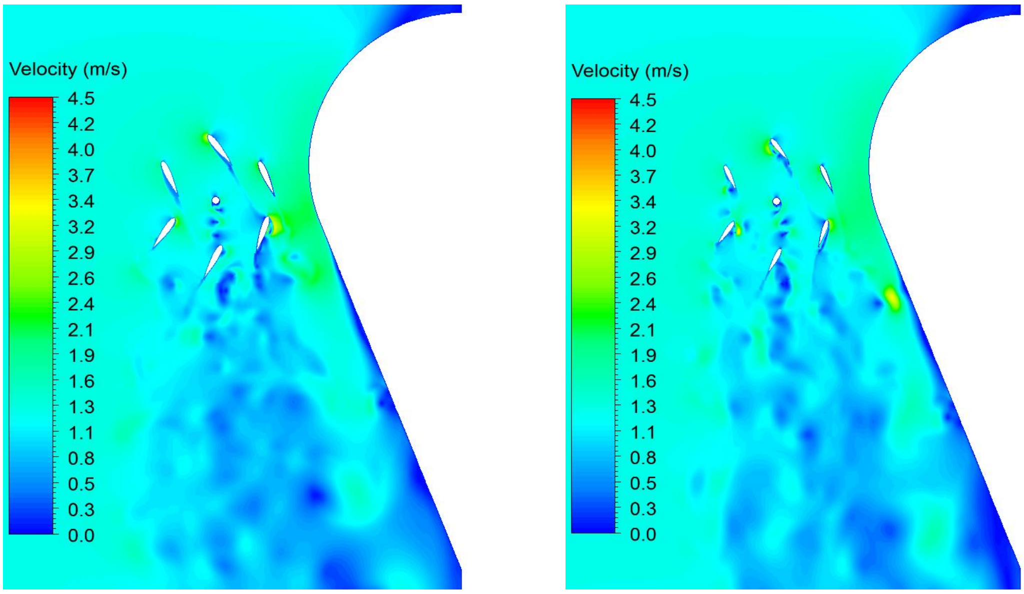

(a) (b)

Figure 30: Turbine consisting of hydrofoil chord lengths of length **(a)** 0.2 m and **(b)** 0.15 m.

5. Discussion

The sliding mesh technique for *mesh motion* has been utilised to facilitate nesting sliding meshes and enable CFD modelling and assessment of a novel tidal turbine. The final mesh contains a total of eight different domains including seven rotating domains. Independent blade pitching has been incorporated into the model via a UDF to control the rotation of the blade meshes. This UDF enables the blades to pitch precisely in the same manner as the scale experimental device. This technique could be applied to other variable-pitch turbines and also various other types of turbomachinery.

A mesh and time-step independent solution were achieved through the use of sensitivity studies and the Richardson extrapolation. As mentioned, it was not possible to carry out a sensitivity study on the domain diameter sizing. Previous studies (Castelli et al. 2010; Mannion, et al. 2018b) have shown that results can be affected by the size of the rotating domain relative to the turbine diameter; these studies recommend a rotating domain of at least 1.5 times the turbine diameter for accurate results. In the current research, a rotating domain of precisely 1.5 times the turbine diameter was used, and acceptable agreement between the experimental and model data was achieved.

The CFD-predicted power coefficients correlate closely with the experimental test data, particularly in the case of the Transitional SST turbulence model. Previous published 2D CFD models attribute over-prediction of turbine performance to blade tip end effects and a higher blockage ratio than in reality **[23, 34]**. When blockage was unaccounted for, $C_{\mathrm{P}max}$ prediction was overestimated by over 100 %, and optimum TSR was twice the measured value.

When comparing the modelled velocities to the LDV measured experimental data, in general, the Transitional SST model outperformed the fully turbulent $k-\omega$ SST model. This is likely due to the abilities of the Transitional SST model over the $k-\omega$ SST model when modelling the transition phase from laminar to turbulent flow. The transitional SST model is therefore recommended for future use in the CFD modelling of vertical axis tidal turbines.

Several design case investigation studies were conducted using the presented validated model. Investigation of the positioning of the turbine relative to the bluff body suggests that the current turbine position is optimal. When the turbine was positioned further downstream, the performance dropped off, particularly at higher rotational speeds. Investigation of shaft sizing confirmed, as expected that larger shafts are detrimental to turbine performance. A trade-off is therefore necessary in regards selection of the optimum shaft diameter; one must choose between greater structural integrity (stiffness and strength) on the one hand and better power performance on the other hand.

Investigation of variable versus fixed pitch design cases showed that including a pitching regime has had a positive effect on the device performance for the 6-blade case with $C_{\mathrm{P}max}$ being 60 % greater compared to a 0° fixed pitch device and occurring at a lower λ value. The current blade pitch control regime had been optimised for peak performance to be achieved at a low TSR value (less than 0.5). As a result, the 3-blade variable-pitch case had insufficient interaction with the flow at this low rotational speed, and significantly lower performance was observed. A different pitch control scheme would be required to properly access the benefits of the 3-blade case.

The 3-blade 0^{o} fixed pitched case achieved a $C_{\mathrm{P}max}$ that was 5 % higher than that of the 6-blade variable-pitch case thus potentially showing it be a more preferred design. In addition to the improved performance, there would also be lower manufacturing and maintenance costs associated with a 3-bladed fixed pitch device due to the lower number of blades and omission of a pitch control mechanism. However, the optimum rotational velocity of the 3-bladed case is more than three times higher than that of the 6-blade variable-pitch case; this is significant in relation to environmental impacts since lower operating TSR values are more environmentally desirable as they reduce the risk of fish and/or animal strikes. The downstream velocity contour maps also show that the 3-bladed case results in higher velocity deficits and therefore a more persistent wake. This is significant in relation to the potential proximity of downstream devices in an array.

The results from the blade chord length investigation showed a 50 mm shorter blade chord length resulted in a lower $C_{\mathrm{P}max}$ value ($\Delta C_{\mathrm{P}max} = 0.04$). Vertical axis turbines extract the majority of power in approximately the first 120^{o} of azimuthal rotation (measured from the turbine axis perpendicular to the ambient flow). The shorter chord length blade means less interaction of the blades with the flow as they are passing through this critical region at the upstream end of the turbine, resulting in lower overall turbine performance. This area is also where the highest flow accelerations are observed for the current device; it is therefore paramount that high blade-flow interactions occur in this region without causing excessive flow retardation and blockage.

6. Conclusion

A two dimensional CFD model of a novel vertical axis turbine has been developed, successfully incorporating the key design aspects of flow acceleration and blade pitch control. This was achieved via a complicated nested sliding mesh technique to allow independent rotation of the turbine and pitching of the blades. The blade mesh motion is controlled through a user-defined function to represent the blade pitch control of each of the six blades independently. A methodology for achieving a mesh and time-independent solution was presented. The following conclusions are drawn from the research results:

- The Transitional model is the most suitable turbulence model for CFD modelling of vertical axis turbines. It was shown to be more accurate than the $k-\omega$ SST model for both performance prediction and wake characterisation.
- Strict convergence criteria must be employed if accurate, and completely independent (both temporally and spatially) results are to be obtained from CFD turbine models. An average torque threshold of $\overline{\Delta T}$ < 0.1 % between one rotation and the next for convergence assessment is recommended as it was shown to produce accurate model results.
- The detailed nested sliding mesh approach developed here could be adopted for other CFD studies of variable-pitch turbines or turbomachinery with complex moving parts.
- Model investigation of the different design cases has confirmed that implementing blade pitch control has had a positive effect on device performance (for a six blade case) in the present design compared with the use of a similar fixed pitch turbine. Pitch control can also be utilised to reduce the operating TSR of the device where there are environmental concerns while maintaining good performance.

Funding: This material is based upon works supported by Science Foundation Ireland under Grant No. 12/RC/2302 through MaREI, the national centre for Marine and Renewable Energy Ireland.

Acknowledgements: The authors wish to acknowledge the DJEI/DES/SFI/HEA Irish Centre for High-End Computing (ICHEC) for the provision of computational facilities and support.

The authors also wish to acknowledge the contribution of Dr Ciaran Kennedy to the experimental testing of the device.

References

Almohammadi, K.M., Ingham, D.B., Ma, L., Pourkashan, M., 2013. Computational fluid dynamics (CFD) mesh independency techniques for a straight blade vertical axis wind turbine. Energy 58, 483–493. doi /10.1016/j.energy.2013.06.012

Almohammadi, K.M., Ingham, D.B., Ma, L., Pourkashanian, M., 2012. CFD Sensitivity Analysis of a Straight-Blade Vertical Axis Wind Turbine. Wind Eng. 36, 571–588. doi/10.1260/0309-524X.36.5.571

ANSYS Fluent 17.1 theory guide, 2016. ANSYS Fluent 17.1 theory guide, Ansys Inc. doi /10.1016/0140-3664(87)90311-2

Bachant, P., Wosnik, M., 2016. Modeling the near-wake of a vertical-axis cross-flow turbine with 2-D and 3-D RANS. J. Renew. Sustain. Energy 8. doi /10.1063/1.4966161

Balduzzi, F., Bianchini, A., Maleci, R., Ferrara, G., Ferrari, L., 2016. Critical issues in the CFD simulation of Darrieus wind turbines. Renew. Energy 85, 419–435. doi /10.1016/j.renene.2015.06.048

Bianchini, A., Balduzzi, F., Bachant, P., Ferrara, G., Ferrari, L., 2017. Effectiveness of two-dimensional CFD simulations for Darrieus VAWTs: a combined numerical and experimental assessment. Energy Convers. Manag. 136, 318–328. doi/10.1016/j.enconman.2017.01.026

Castelli, M.R., Ardizzon, G., Battisti, L., Benini, E., Pavesi, G., 2010. Modeling strategy and numerical validation for a Darrieus vertical axis micro-wind turbine. Proc. ASME 2010 Int. Mech. Eng. Congr. Expo. IMECE2010 1–10.

Chatterjee, P., Laoulache, R.N., 2013. Performance Modeling of Ducted Vertical Axis Turbine Using Computational Fluid Dynamics. Mar. Technol. Soc. J. 47, 36–44. doi/10.4031/MTSJ.47.4.12

Ghasemian, M., Nejat, A., 2015. Aero-acoustics prediction of a vertical axis wind turbine using Large Eddy Simulation and acoustic analogy. Energy 88, 711–717. doi/10.1016/j.energy.2015.05.098

Glauert, H., 1926. A General Theory of the Autogyro. Sci. Res. Air Minist. - Reports Memo. No. 1111 41.

Gupta, S., Leishman, J.G., 2005. Comparison of Momentum and Vortex Methods for the Aerodynamic Analysis of Wind Turbines. 43rd AIAA Aerosp. Sci. Meet. Exhib. AIAA 2005-, 1–24. doi/10.2514/6.2005-594

Klimas, P.C., Sheldahl, R.E., 1978. Four Aerodynamic Prediction Schemes for Vertical-Axis: A Compendium SAND78-0014. 1978.

Korobenko, a., Hsu, M.-C., Akkerman, I., Bazilevs, Y., 2013. Aerodynamic Simulation of Vertical-Axis Wind Turbines. J. Appl. Mech. 81, 021011. doi/10.1115/1.4024415

Lain, S., Osorio, C., 2010. Simulation and evaluation of a straight-bladed darrieus-type cross flow marine turbine. J. Sci. Ind. Res. (India). 69, 906–912.

Lam, H.F., Peng, H.Y., 2016. Study of wake characteristics of a vertical axis wind turbine by two- and three-dimensional computational fluid dynamics simulations. Renew. Energy 90, 386–398. doi/10.1016/j.renene.2016.01.011

Langtry, R.B., Menter, F.R., 2009. Correlation-Based Transition Modeling for Unstructured Parallelized Computational Fluid Dynamics Codes. AIAA J. 47, 2894–2906. doi/10.2514/1.42362

Launder, B.E., Spalding, D.B., 1974. The numerical computation of turbulent flows. Comput. Methods Appl. Mech. Eng. 3, 269–289. doi/10.1016/0045-7825(74)90029-2

Lee, N.J., Kim, I.C., Kim, C.G., Hyun, B.S., Lee, Y.H., 2015. Performance study on a counter-rotating tidal current turbine by CFD and model experimentation. Renew. Energy 79, 122–126. doi/10.1016/j.renene.2014.11.022

Maître, T., Amet, E., Pellone, C., 2013. Modeling of the flow in a Darrieus water turbine: Wall grid refinement analysis and comparison with experiments. Renew. Energy 51, 497–512. doi/10.1016/j.renene.2012.09.030

Mannion, B., Leen, S.B., Nash, S., 2018a. A two and three-dimensional CFD investigation into performance prediction and wake characterisation of a vertical axis turbine. J. Renew. Sustain. Energy 10, 34503. doi/10.1063/1.5017827

Mannion, B., McCormack, V., Kennedy, C., Leen, S.B., Nash, S., 2018b. An experimental study of a flow-accelerating hydrokinetic device. Proc. Inst. Mech. Eng. Part A J. Power Energy 095765091877262. doi/10.1177/0957650918772626

Masters, I., Williams, A., Croft, T.N., Togneri, M., Edmunds, M., Zangiabadi, E., Fairley, I., Karunarathna, H., 2015. A comparison of numerical modelling techniques for tidal stream turbine analysis. Energies 8, 7833–7853. doi/10.3390/en8087833

Menter, F.R., 1994. 2-Equation eddy-visocity turbulence models for engineering applications. Aiaa J. 32, 1598–1605. doi/10.2514/3.12149

Menter, F.R., Langtry, R.B., Likki, S.R., Suzen, Y.B., Huang, P.G., Volker, S., 2006. A Correlation-Based Transition Model Using Local Variables - Part I: Model Formulation. J. Turbomach. 128, 413. doi/10.1115/1.2184352

Mohamed, M.H., 2012. Performance investigation of H-rotor Darrieus turbine with new airfoil shapes. Energy 47, 522–530. doi/10.1016/j.energy.2012.08.044

Paraschivoiu, I., Delclaux, F., Fraunié, P., Béguier, C., 1983. Aerodynamic Analysis of the Darrieus Wind Turbines Including Secondary Effects. J. Energy 7, 416–422.

Ponta, F.L., Jacovkis, P.M., 2001. A vortex model for Darrieus turbine using finite element techniques. Renew. Energy 24, 1–18. doi/10.1016/S0960-1481(00)00190-7

Rossetti, A., Pavesi, G., 2013. Comparison of different numerical approaches to the study of the H-Darrieus turbines start-up. Renew. Energy 50, 7–19. doi/10.1016/j.renene.2012.06.025

Sheldahl, R.E., Klimas, P.C., 1981. Aerodynamic characteristics of seven symmetrical airfoil sections through 180-degree angle of attack for use in aerodynamic analysis of vertical axis wind turbines. Technical Report SAND80-2114, Sandia National Laboratories. Tech. SAND80-2114, Sandia Natl. Lab. doi/10.2172/6548367

Spalart, P.R., Allmaras, S.R., Reno, J., 1992. A One-Equatlon Turbulence Model for Aerodynamic Flows Boeing Commercial Airplane Group 30th Aerospace Sciences. AIAA Pap. 1992-0439. doi/10.2514/6.1992-439

Strickland, J., 1975. The Darrieus Turbine, A Performance Prediction Method Using Multiple Stream Tubes. Sandia Lab. SAND. doi/SAND75-0431

Strickland, J.H., Webster, B.T., Nguyen, T., 1979. A Vortex Model of the Darrieus Turbine: An Analytical and Experimental Study. J. Fluids Eng. 101, 500. doi/10.1115/1.3449018

Templin, R.J., 1974. Aerodynamic performance theory for the NRC vertical-axis wind turbine. NASA STI/Recon Tech. Rep. N 7616618 76, 16618.

Trivellato, F., Raciti Castelli, M., 2014. On the Courant-Friedrichs-Lewy criterion of rotating grids in 2D vertical-axis wind turbine analysis. Renew. Energy 62, 53–62. doi/10.1016/j.renene.2013.06.022

Wilcox, D.C., 1988. Reassessment of the scale-determining equation for advanced turbulence models. AIAA J. 26, 1299–1310. doi/10.2514/3.10041